



HAL
open science

Comparisons of Different Propeller Wake Models for a Propeller-Wing Combination

Yuchen Leng, Murat Bronz, Thierry Jardin, Jean-Marc Moschetta

► **To cite this version:**

Yuchen Leng, Murat Bronz, Thierry Jardin, Jean-Marc Moschetta. Comparisons of Different Propeller Wake Models for a Propeller-Wing Combination. 8th European Conference for Aeronautics and Space Sciences, Jul 2019, Madrid, Spain. pp.0. hal-03385864

HAL Id: hal-03385864

<https://hal.science/hal-03385864>

Submitted on 19 Oct 2021

HAL is a multi-disciplinary open access archive for the deposit and dissemination of scientific research documents, whether they are published or not. The documents may come from teaching and research institutions in France or abroad, or from public or private research centers.

L'archive ouverte pluridisciplinaire **HAL**, est destinée au dépôt et à la diffusion de documents scientifiques de niveau recherche, publiés ou non, émanant des établissements d'enseignement et de recherche français ou étrangers, des laboratoires publics ou privés.



Open Archive Toulouse Archive Ouverte (OATAO)

OATAO is an open access repository that collects the work of some Toulouse researchers and makes it freely available over the web where possible.

This is an author's version published in: <https://oatao.univ-toulouse.fr/28446>

Official URL:

To cite this version :

Leng, Yuchen and Bronz, Murat and Jardin, Thierry and Moschetta, Jean-Marc Comparisons of Different Propeller Wake Models for a Propeller-Wing Combination. (2019) In: 8th European Conference for Aeronautics and Space Sciences, 1 July 2019 - 4 July 2019 (Madrid, Spain).

Any correspondence concerning this service should be sent to the repository administrator:

tech-oatao@listes-diff.inp-toulouse.fr

Comparisons of Different Propeller Wake Models for a Propeller-Wing Combination

Yuchen Leng¹, Murat Bronz², Thierry Jardin¹ and Jean-Marc Moschetta¹

¹ISAE-SUPAERO, Université de Toulouse, France

Yuchen.Leng@isae-supaero.fr

²ENAC, Université de Toulouse, France

Abstract

A detailed experimental study of propeller-wing interaction was presented. Five-hole probe was used to obtain velocity distribution at a survey plane behind trailing edge of a high-aspect-ratio wing with tractor propeller. Significant deformation of propeller slipstream was observed compared to a free propeller. The deformation was more prominent at low advance ratio, where transition flight of vertical take-off / landing aircraft were concerned. Comparison with two recent reduced-order slipstream models revealed large discrepancies between theoretical predictions and wake survey results. An analytical model of slipstream transverse deformation was proposed at the end that might be incorporated into improve such models.

1. Introduction

Recent development in aviation has seen increasing interests in electrical vertical take-off and landing (eVTOL) aircraft for a wide range of applications (Figure 1a, 1b). Major challenges of eVTOL is related to its flight dynamics at near hover condition. At low airspeed, the lifting capability and efficiency of aerodynamic surfaces are reduced. A powered-lifting system utilizing propeller or fan thrust was generally considered for safe operation in low-speed regime.¹ Blown wing is one of the promising designs in this category : a tractor propeller is installed in front of the wing such that its energized slipstream augments wing lift and restores aerodynamic moment of control surfaces. Despite various past studies on propeller loads at low speed transition flight,²⁻⁴ to predict the performance of propeller-wing combination during preliminary design, a rapid estimation of the slipstream effect must be included.



(a) ISAE MAVION⁵



(b) ENAC Cyclone⁶

Figure 1: VTOL aircraft concepts

The slipstream is characterised by a near-wake contraction region dominated by pressure driven acceleration and followed by a far-wake expansion region caused by the mixing with external flow. A circumferential swirl component about centreline is also induced by the rotation of blades. Both axial and swirl components are important for performance analysis as the effective flow speed and angle of attack of the wing are altered at blown sections.

Currently, there exist several reduced-order models to describe the accelerating flow after a free propeller.^{7,8} Khan et al⁹ have developed a semi-empirical model capable of predicting streamtube expansion in far downstream region. A similar model has also been presented by Goates¹⁰ based on studies of turbulent jet mixing.

Khan et al modelled the slipstream development according to empirical model derived from jet mixing and marine propellers. The flow region was divided into three region as shown in Figure 2 : near-field region (contraction), zone of flow establishment (ZFE) and zone of established flow (ZEF). In ZEF, the flow reaches a self-similar Gaussian velocity profile and ZFE is a transition zone. Model coefficients were fitted with small-scale aircraft propeller experiment. No swirl was considered.

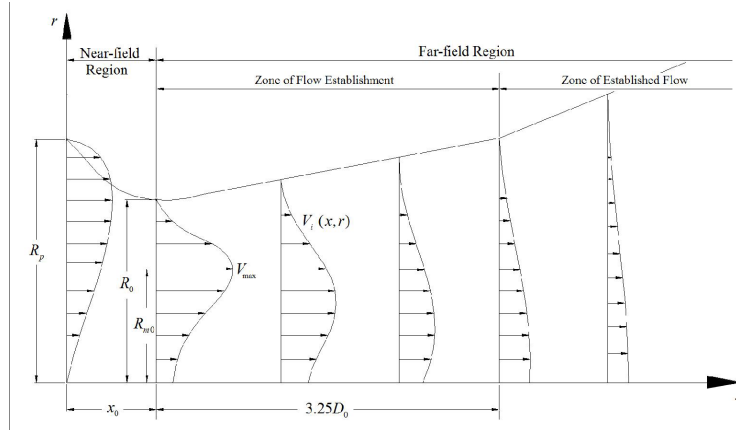


Figure 2: Three-region slipstream model (reproduced from Khan et al⁹)

A more recent model from Goates et al¹⁰ had a similar three-region model. Instead of prescribing the shape of flow expansion in ZFE and ZEF, momentum conservation and flow diffusion rate was calculated to resolve wake development. Swirl velocity was also included, and a self-similar double-segment linear profile was assumed at ZFE.

The two models have been validated for wake measurements of independent propeller. However their accuracies for a propeller-wing combination haven't been extensively studied. In the presence of a wing, past studies have pointed out a mutual influence between propeller and the lifting surface. Veldhuis et al.^{11,12} pointed out the reduction in slipstream velocity to be critical in estimating correct lift and drag characteristics of propeller-wing combination. To investigate the accuracy of existing models, a low-speed wake survey has been conducted in ENAC research wind tunnel with a five-hole probe to measure the axial and tangential velocity. The measurement concentrates around the slipstream near the trailing edge of a propeller-wing combination, which consisted of a semi-span wing equipped with a simple flap and a tractor propeller fixed at mid-span. Different advance ratios and rotation speeds were tested.

2. Test Set-up

The experiment was conducted at ENAC low-speed wind tunnel as presented in Figure 3. The test section has a cross-section dimension of $500mm \times 500mm$ and length of $1200mm$. The test section was open on both sides while walls were presented at the top and bottom.

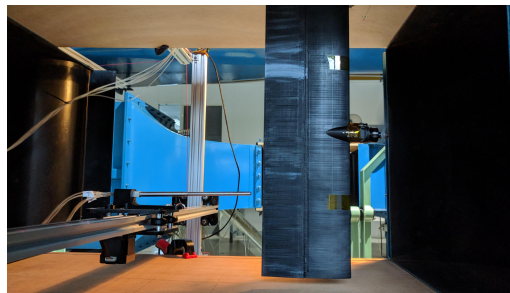


Figure 3: Experimental set-up at ENAC low-speed wind tunnel

The wing section has a $500mm$ semi-span and constant chord length of $150mm$, which equals an aspect ratio of 6.67 for the full wing. *NACA0012* aerofoil was used as wing cross section. The top wall of test section served as a plane of symmetry. The last 50% chord was built as a full-span flap, although only results for neutral flap position is presented in this paper.

A single propeller was attached to a nacelle located at $250mm$ from plane of symmetry, and rotor disk plane was $55mm$ ahead of leading edge. Propeller used during the test was an APC 3-blade $5 \times 4.6E$ propeller.

During test, the wing was considered to be a right-hand wing, and coordinate systems were defined with origin at propeller disk centre. X -axis lies along rotation axis pointing upstream and Y -axis is in the spanwise direction pointing towards wingtip. The coordinate system is illustrated in Figure 4.

A 2-degree-of-freedom linear motion system was constructed for conducting the wake survey. A rectangular

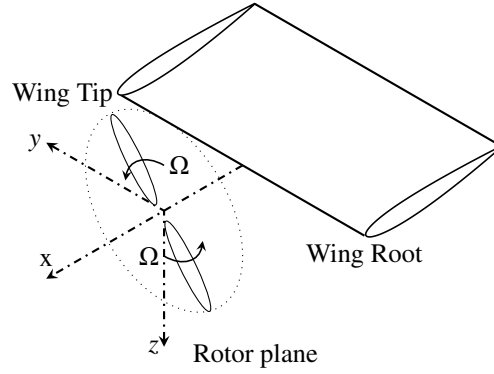


Figure 4: Slipstream coordinate system (not to scale)

aluminium frame surrounded an area perpendicular to freestream direction. Edges of the frame contained rail where two stepper motors were installed along the vertical segments for ascending and descending motions. The two motors were synchronised and they bore a horizontal rail that another stepper motor moved along and carried a cart with flow measurement probe.

The probe used for wake survey was a 5-hole Aeroprobe. The probe head was situated 15mm behind trailing edge, and thus defined a survey plane S located 1.7 times propeller diameter downstream the rotor centre. It had been previously calibrated in the wind tunnel using a non-nulling method similar to the one of Reichert et al.¹³ The probe is thus capable of providing highly accurate measurement on flow velocity. The result was taken in a 3-second period at 700Hz sampling frequency. For performance analysis, the blade passing frequency is significantly larger than the frequency of airframe motions, and thus only time-averaged results are of interest.

The test was conducted in three different advance ratios defined as

$$J = \frac{V_\infty}{nD} \quad (1)$$

where V_∞ is freestream speed, n is rotation speed in round per second and D is propeller diameter (0.127m). For each advance ratio, three different rotation speeds were used at 6000rpm , 8000rpm and 10000rpm to investigate Reynolds number effect. The complete test matrix is tabulated in Table 1.

 Table 1: Test V_∞ for different rotation speeds and advance ratios

J	6000RPM	8000RPM	10000RPM
0.25	3.2m/s	5.1m/s	7.6m/s
0.40	4.2m/s	6.8m/s	10.1m/s
0.60	5.2m/s	8.5m/s	12.7m/s

During the test, appropriate rotation speed and freestream velocity were first set. Motion control system was then started to sample flow velocity of different points in the survey plane. Stepper motors were controlled in an alternating pattern to cover a 15×15 grid. At each point, a 1s delay was programmed before acquisition to remove unsteady effect of probe movement.

Measured velocity was then decomposed in directions along and perpendicular to freestream flow, which were designated as streamwise flow u and transverse flow v_t .

3. Wake Survey at Downstream Plane

In this section, wake survey at test conditions is presented in the form of streamwise speed contour and transverse velocity field. A qualitative description will first be presented to discuss the effect of advance ratio on propeller slipstream development. It is then followed by quantitative comparisons of two slipstream models.

3.1 Effect of different advance ratios

Flow field at survey plane for 8000RPM rotation speed is presented in Figure 5. Horizontal and vertical axes take origin at rotor centre and the coordinates are normalised by propeller radius.

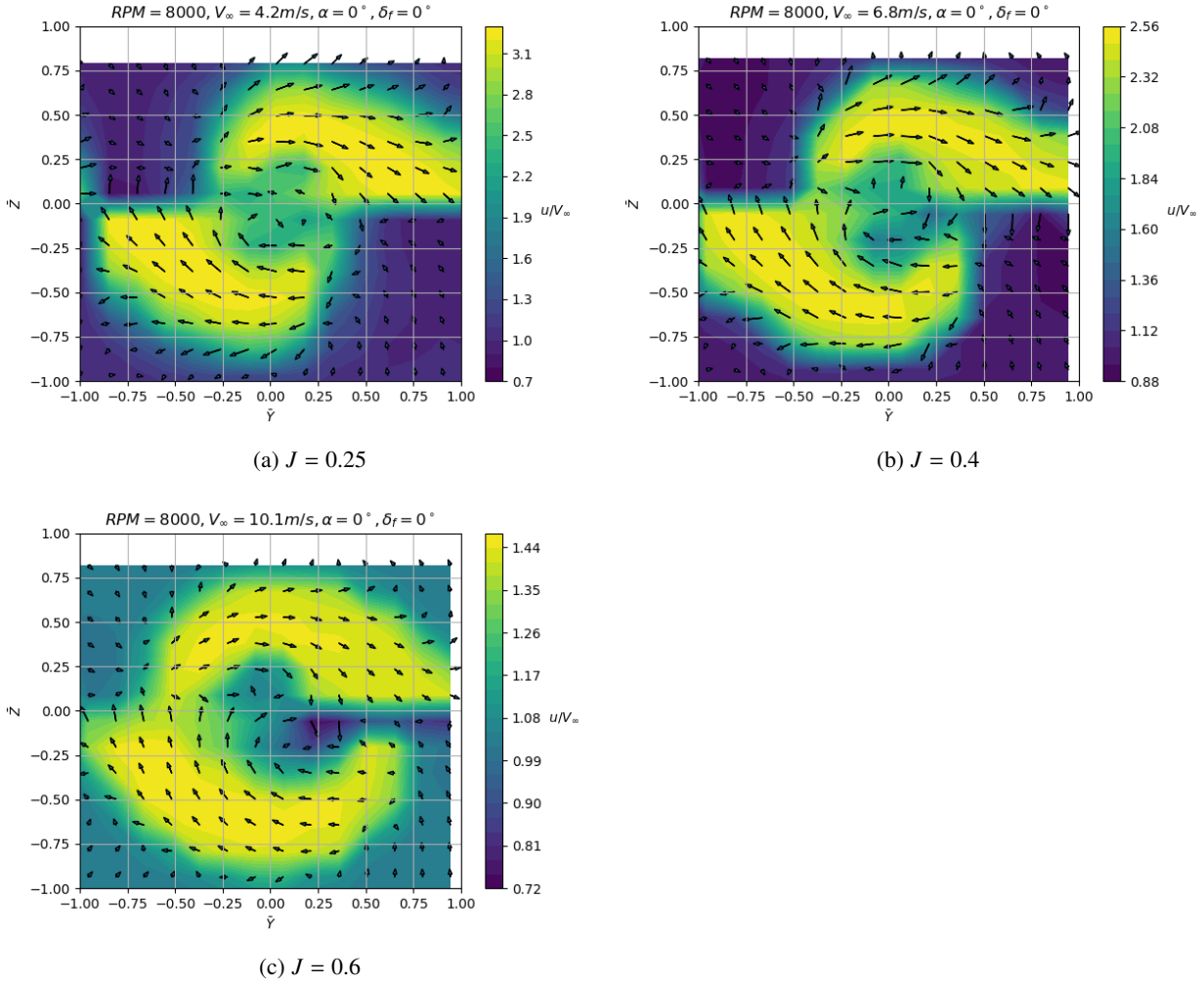


Figure 5: Wake survey after propeller-wing combinations at various advance ratios

The smallest advance ratio $J = 0.25$ corresponds to the flow pattern depicted in Figure 5a, where a distinctive difference from the cylindrical slipstream can be observed. This deformation is closely related with the presence of wing section, which is at $\bar{z} = 0$. Above the wing upper surface ($\bar{z} > 0$), the high speed region of streamwise flow is concentrated in the right half of the figure. The opposite is true for the flow region underneath the wing, where the accelerated flow can be found on the left hand side. Because of this difference between upper and lower portion of survey plane, a drastic change in flow speed took place at $\bar{z} = 0$ and $|\bar{y}| > 0.25$: behind the upgoing blade ($\bar{y} < -0.25$), streamwise speed decreases when going upward across the wing; behind downgoing blade ($\bar{y} > 0.25$), streamwise speed increases when going upward across the wing.

The transverse velocity field mainly follows the direction of blade rotation and represents a loss of energy.⁸ A similar distinctive change of velocity is also present behind the wing, where the swirling motion is almost restricted to the flow regime opposed to the rotation direction.

With the increase of freestream velocity, in Figure 5b and 5c, the wing influenced region, where distinctive velocity change is observed after the wing, starts to reduce. At $J = 0.25$, as mentioned before, the influenced region begins at around $|\bar{y}| = 0.25$. It moves to $|\bar{y}| = 0.35$ and 0.6 for $J = 0.4$ and 0.6 respectively. Therefore as the advance ratio increases, the deformation of slipstream due to presence of wing reduces, and the slipstream approaches to ideal cylindrical shape.

The cause of this phenomenon can be attributed to multiple factors. Local stall and transverse slipstream displacement were believed to be the main reasons. Local angle of attack induced by axial acceleration and swirl motion within slipstream may be estimated by general momentum theory.¹⁴ At $J = 0.25$, the local angle of attack may reach $15.3 - 22.3^\circ$ for wing section located between $0.25 < |\bar{y}| < 1$, which is above 12° critical angle of attack for NACA0012 aerofoil at comparable Reynolds number. The stationary flow presented on suction side of stalled aerofoil may create

the observed low-speed region.

While local stall explained the low-speed region existed at low advance ratio, it doesn't explain the stretch of high-speed region in spanwise direction. Furthermore, local angle of attack estimated for $J = 0.6$ is below critical angle of attack. Wake deformation at this advance ratio may be attributed to transverse wake displacement first qualitatively observed by Witkowski et al,¹⁵ and will be further explained in section 4.

3.2 Reynolds number effect

Figure 6 demonstrates wake surveys at three tested rotation speeds for various advance ratios. Only streamwise speed contours were plotted for clarity, and they were overlaid on top of each other in different line styles for comparison.

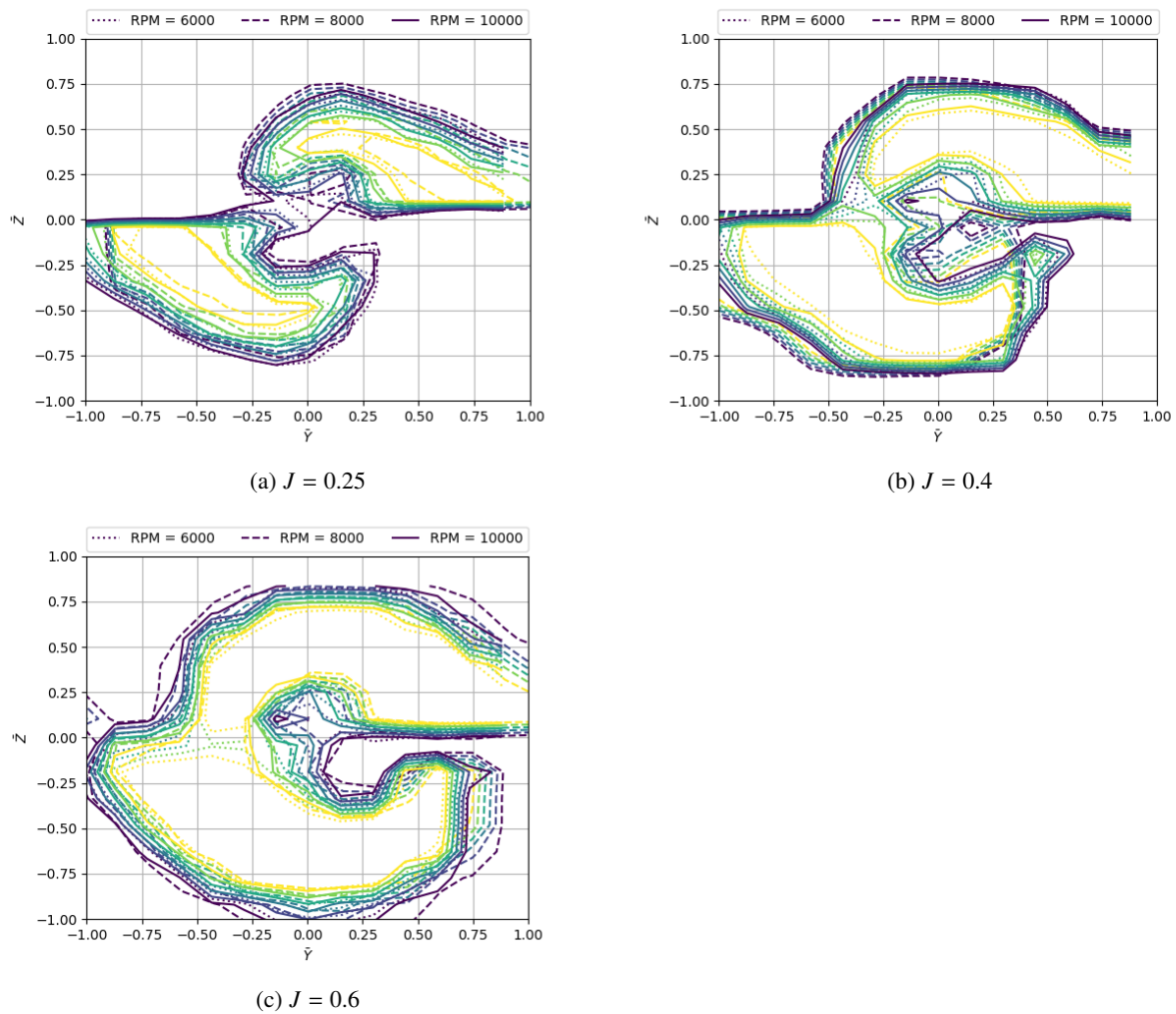


Figure 6: Effect of Reynolds number on slipstream development at various advance ratios

At all three advance ratios, the velocity contours lie close to each other when plotted at the same levels. This suggests that the slipstream development isn't subject to significant Reynolds number effect at test conditions, and thus the advance ratio remains as dominant parameter. Subsequent discussions will be primarily based on measurement at $8000rpm$.

3.3 Comparison with model from Khan et al⁹

Streamwise velocity distribution at downstream plane is plotted against numerical slipstream model from Khan et al in Figure 7. The numerical results were calculated using propeller data from manufacturer¹⁶ in test conditions. The plots are presented as contour lines sampled at the same levels.

As mentioned before, the semi-empirical model only considers independent propeller and thus the calculated streamwise speed contour appears as concentric circles in dashed line. The iso-line radius for the same velocity reduces as advance ratio increases.

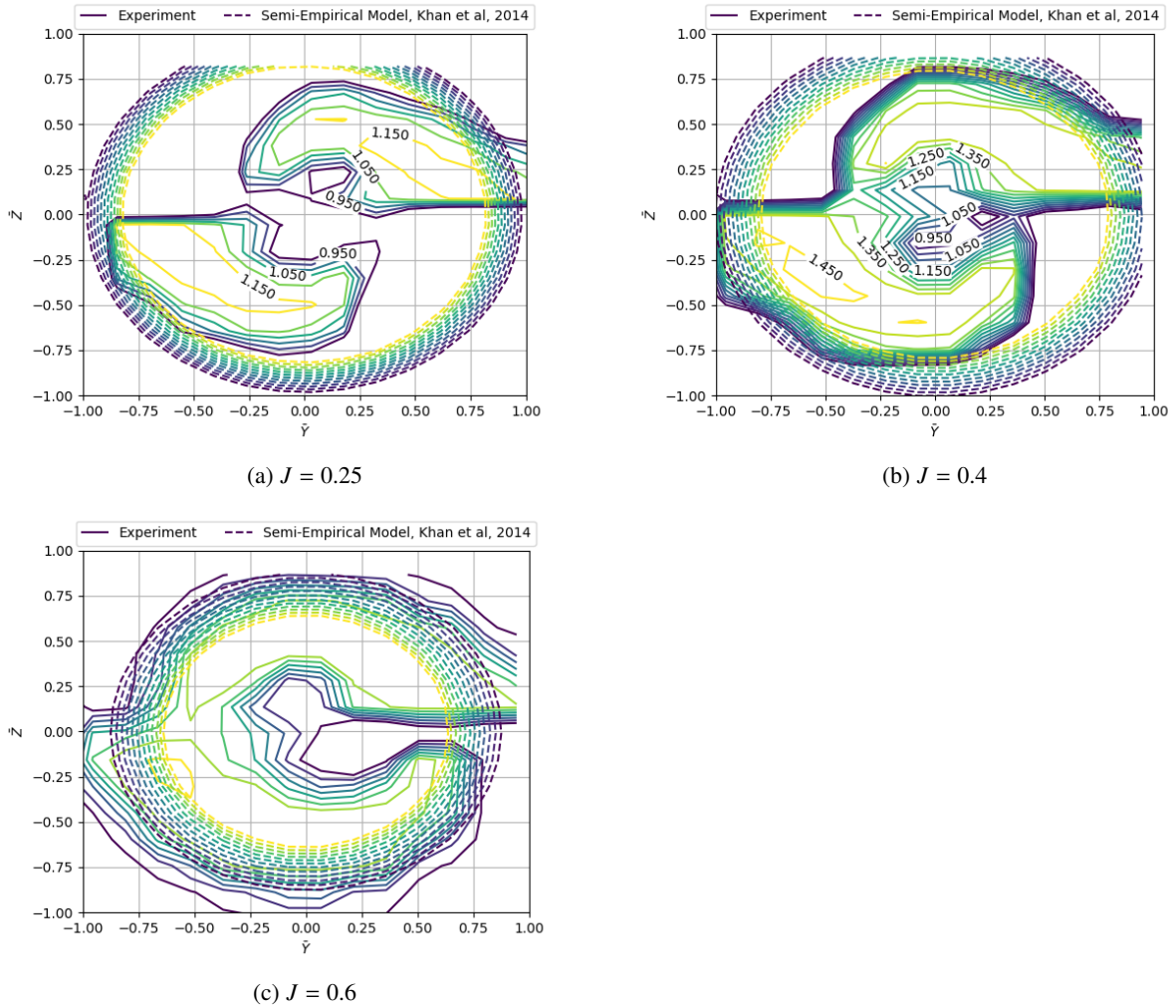


Figure 7: Wake survey after propeller-wing combinations compared with slipstream model from Khan et al⁹

When compared with wake survey of propeller-wing combination, the differences are obvious. The model is axisymmetric, and thus the influence from wing couldn't be included. Consequently transverse slipstream deformation isn't present in predicted results, while it is apparent in wake survey results especially for advance ratios $J = 0.25$ and 0.4 .

Finally, although the radius of contour lines calculated from Khan's model agrees to some extent with the outer boundary of wake surveys at $J = 0.4$ and 0.6 , the contour line radius falls outside of survey result at $J = 0.25$. Wake contraction at heavy loaded condition is thus underestimated.

3.4 Comparison with model from Goates et al¹⁰

Similar comparison is presented in Figure 8 with the slipstream model proposed by Goates et al. The numerical case also included a wing section modelled from lifting-line theory¹⁷ with the same characteristics as the experimental set-up. A measurement of blade chord and twist distribution was conducted to provide input for the blade element momentum model, and thrust results were compared with manufacture data¹⁶ for validation (error within 5%).

Because the model from Goates is based on a blade element method, it is capable of producing a more accurate velocity distribution in radius direction. This is observed from the presence of lower velocity region around propeller hub, which Khan's model failed to produce.

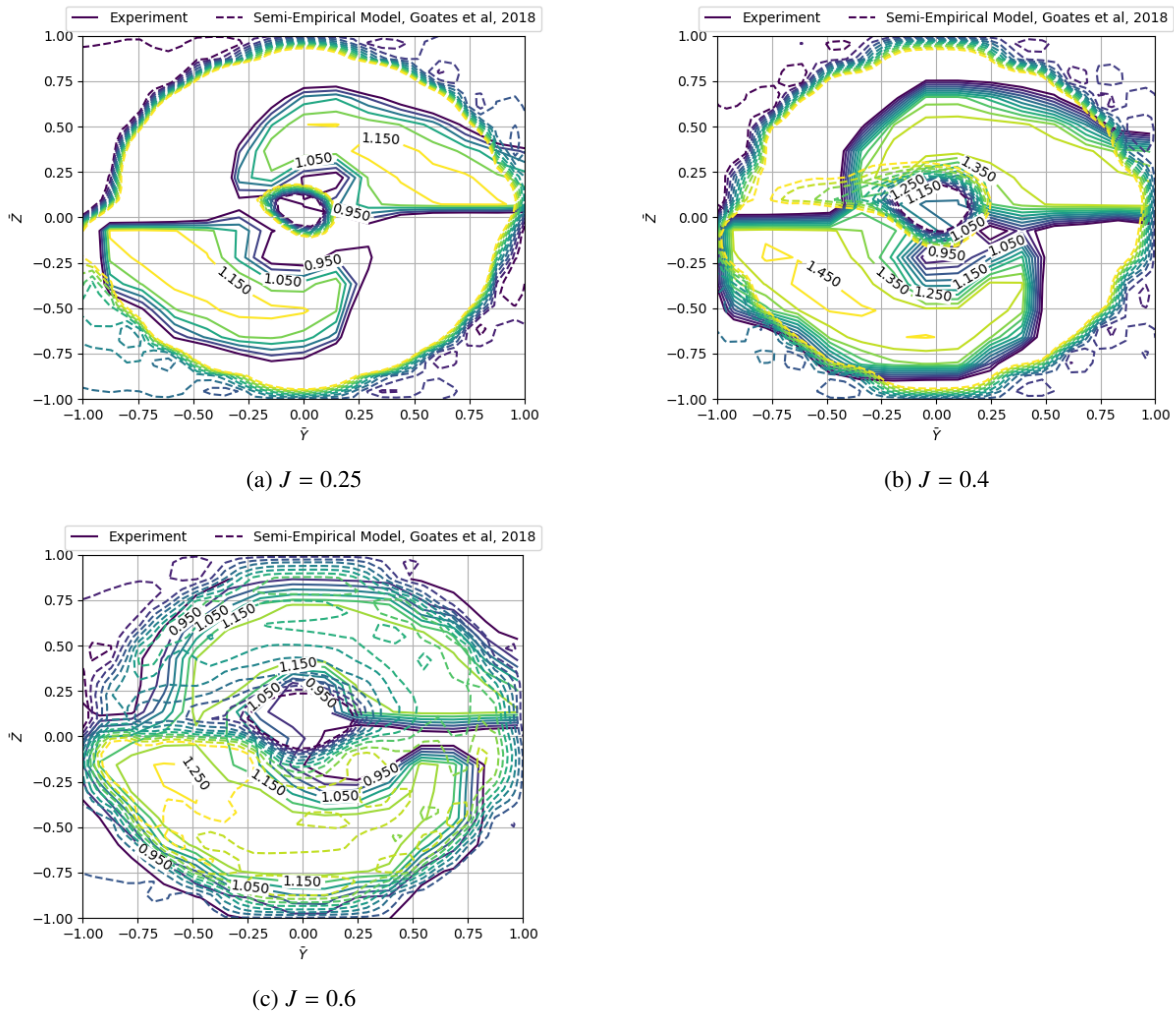


Figure 8: Wake survey after propeller-wing combinations compared with slipstream model from Goates et al¹⁰

The calculated velocity profile also shows a certain degree of asymmetry about propeller axis. It, however, isn't as pronounced as in the wake survey results. In the lifting-line method, only propeller slipstream effects are considered when calculating wing performance, the reciprocal effects are neglected. Therefore, the velocity distribution at survey plane is a combination of undisturbed slipstream velocity and induced velocity from wing horseshoe vortices. The asymmetry in velocity distribution is entirely due to the difference in bound circulations of wing sections after up-going and down-going blades.

4. Analytical Model of Wake Displacement

From flow survey behind propeller-wing combinations introduced in section 3, it has been observed that when separated by the wing, two halves of propeller slipstream were subjected to opposite transverse motions, or "transverse slipstream displacement".

The phenomenon was explained by Witkowski et al¹⁵ using a method of imaginary. They have qualitatively demonstrated that a pair of streamwise vortices mirrored by the wing surface will induce the correct trend of fluid motion. However no quantitative results were given as the effect on a propeller-wing combination at high speed condition was estimated to be small.

However such phenomenon is significant at low-speed regime, observed in section 3. From the comparisons with two recently developed reduced-order models, the phenomenon hasn't been included in performance estimation of propeller-wing combinations.

To include the transverse displacement in a potential model isn't trivial. Consider the deformed slipstream system in figure 9 where a series of vortex rings symbolise the blade tip vortices shed from one propeller blade. The vortex

line is displaced in corresponding directions upon contact with the wing.

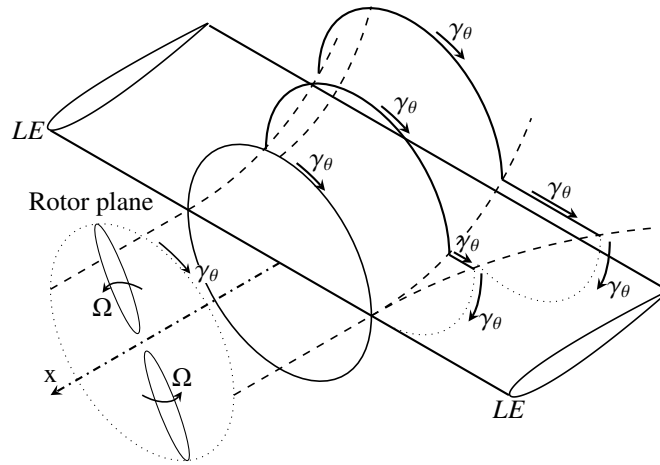


Figure 9: Displaced propeller slipstream and connecting line vortex segments

This simple model shows the upper and lower halves of the helical vortex severed and moving in their respective directions. Such model isn't admissible in potential flow methods. A line vortex is needed to reconnect the ends of upper and lower vortex semi-rings. The addition of the line vortex segment is significant in three ways :

First, it completes the vortex system so that Helmholtz theorem is again respected. The solution is thus admissible in potential methods.

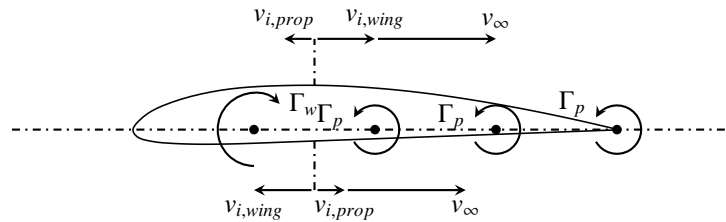


Figure 10: Side view of an aerofoil section after up-going propeller blade

Second, the circulation has physical meaning of streamwise velocity difference between the upper and lower surface. In Figure 10, an aerofoil section after up-going blade is shown. According to Figure 9, at the upper surface, the aerofoil section is situated outside of the propeller slipstream and thus experiences a smaller velocity component in streamwise direction. At lower surface the streamwise component is however augmented because of the induced velocity within propeller slipstream. The velocity difference means additional circulation exists around the aerofoil section.

Third, the direction of the vortex segment has the effect of attenuating the overestimation of propeller-wing interaction. From the previous discussion on Figure 10, the bound line vortex segments add an opposing circulation around the aerofoil. The up-going blade however induces increased local angle-of-attack and thus wing circulation Γ_w is increased. The bound propeller vortex segments therefore work to reduce the effect of Γ_w .

To correctly place the bound vortex segments so that they affect the corresponding wing sections, an estimation of the transverse slipstream displacement is needed. The next sections present a qualitative estimation of centreline deformation for a propeller slipstream on a flat plate.

4.1 Imaginary Distributed Slipstream Vortex Field

When the wing is present, the normal velocity at the lifting surface must vanish. This non-penetration condition can be satisfied by reversing the direction of axial and radial distributed vortex elements. The imaginary system is given in equations 3 - 5, and illustrated in Figure 11. In equations 3 - 5, angle ϕ refers to wake helix angle measured at the propeller rotor plane.

$$\vec{\gamma} = (\gamma_r, \gamma_\theta, \gamma_x) \quad (2)$$

$$\gamma_r = \begin{cases} -\frac{\Gamma_0}{2\pi r} & r \leq R, 0 < \theta < \pi, x = 0 \\ \frac{\Gamma_0}{2\pi r} & r \leq R, \pi < \theta < 2\pi, x = 0 \\ 0 & \text{otherwise} \end{cases} \quad (3)$$

$$\gamma_\theta = \begin{cases} -\frac{\Gamma_0 \cos \phi}{2\pi R} & r = R, x < 0 \\ 0 & \text{otherwise} \end{cases} \quad (4)$$

$$\gamma_x = \begin{cases} \frac{\Gamma_0 \sin \phi}{2\pi R} & r = R, 0 < \theta < \pi, x < 0 \\ -\frac{\Gamma_0 \sin \phi}{2\pi R} & r = R, \pi < \theta < 2\pi, x < 0 \\ 0 & \text{otherwise} \end{cases} \quad (5)$$

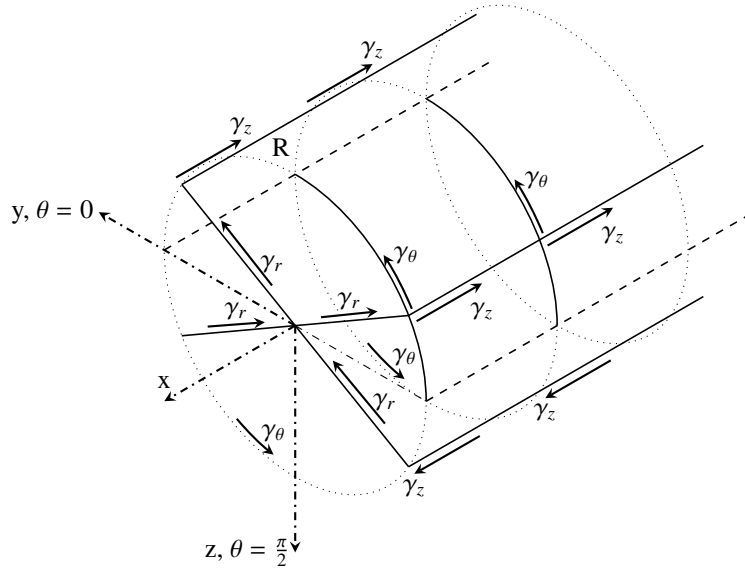


Figure 11: Imaginary propeller distributed vortex system

Notice that circumferential distributed vortices don't change sign, so that Helmholtz theorem at the surface is satisfied. Non-penetration condition is still assured as the circumferential component doesn't induce normal velocity at the surface. The upper half of imaginary distributed vortex system represents the upper propeller slipstream with wing leading edge situated exactly at rotor plane.

It is apparent that the axial induced velocity along centreline doesn't change in the imaginary distributed vortex system. Furthermore, it will be assumed that the induced velocity doesn't vary much around centreline, such that the centreline value could be used to trace the deformed trajectory. During the process, slipstream boundary will remain as a straight semi-infinite cylinder. The problem then reduces into solving centreline transverse induced velocity v_{iy} .

Velocity v_{iy} comes from two parts : a first part induced by rotor plane vortex $v_{iy_{\gamma_r}}$; and a second part from axial vortices in trailing wake $v_{iy_{\gamma_x}}$.

4.1.1 Rotor plane induced transverse velocity $v_{iy_{\gamma_r}}$

At rotor plane where $r \leq R, x = 0$, an elementary vortex segment is expressed in equation 6.

$$d\vec{\Gamma}_r = \gamma_r r d\theta d\hat{r}_r = \mp \frac{\Gamma_0}{2\pi} d\theta d\hat{r}_r = \mp \frac{\Gamma_0}{2\pi} d\theta dr (\cos \theta \hat{i} + \sin \theta \hat{j}) \quad (6)$$

where the expression takes negative sign above the surface ($0 < \theta < \pi$). Because of symmetry, the contribution from vortex elements above the surface is identical as that from below. Thus the induced velocity from upper vortex elements is doubled to obtain the full component.

Relative position vector from an arbitrary downstream position A is given in equation 7.

$$\vec{r}_{\Gamma,A} = r (\cos \theta \hat{i} + \sin \theta \hat{j}) - x_A \hat{k} \quad (7)$$

Differential transverse induced velocity is obtained from Biot-Savart law.

$$dv_{ix_{yr}}(x_A) = \frac{(\vec{r}_{\Gamma,A} \times \vec{\Gamma}_r)_y}{4\pi r_{\Gamma,A}^{3/2}} = -\frac{\Gamma_0 x_A}{8\pi^2} \frac{\sin \theta d\theta dx}{(r^2 + x_A^2)^{3/2}} \quad (8)$$

Integrate on the upper half rotor plane and double the result, the transverse induced velocity from rotor plane vortex distribution is obtained.

$$v_{iy_{yr}}(x_A) = -\frac{\Gamma_0 x_A}{4\pi^2} \int_0^R \int_\pi^{2\pi} \frac{\sin \theta d\theta dr}{(r^2 + x_A^2)^{3/2}} = -\frac{\Gamma_0 x_A}{2\pi^2} \int_0^R \frac{dr}{(r^2 + x_A^2)^{3/2}} \quad (9)$$

$$v_{iy_{yr}}(\bar{x}_A) = -\frac{\Gamma_0}{2\pi^2 R} \frac{1}{\bar{x}_A \sqrt{1 + \bar{x}_A^2}} \quad (10)$$

4.1.2 Trailing wake induced transverse velocity $v_{iy_{yx}}$

At wake boundary where $r = R, x < 0$, streamwise elementary vortex segment is expressed in equation 11.

$$d\vec{\Gamma}_x = \gamma_x R d\theta d\hat{x}_x = \pm \frac{\Gamma_0 \sin \phi}{2\pi} d\theta d\hat{x}_x = \pm \frac{\Gamma_0 \sin \phi}{2\pi} d\theta dx \hat{k} \quad (11)$$

where the expression takes negative sign above the surface ($\pi < \theta < 2\pi$). Similar to the situation with rotor plane induced velocity, the result from upper vortex elements is doubled to obtain full component of transverse induced velocity.

Relative position vector from an arbitrary downstream position A is given in equation 12.

$$\vec{r}_{\Gamma,xA} = R (\cos \theta \hat{i} + \sin \theta \hat{j}) + (x - x_A) \hat{k} \quad (12)$$

Differential transverse induced velocity is obtained from Biot-Savart law.

$$dv_{ix_{yx}}(x_A) = \frac{(\vec{r}_{\Gamma,xA} \times \vec{\Gamma}_x)_y}{4\pi r_{\Gamma,xA}^{3/2}} = \frac{\Gamma_0 R \sin \phi}{8\pi^2} \frac{\sin \theta d\theta dx}{[R^2 + (x - x_A)^2]^{3/2}} \quad (13)$$

Integrate on the upper semi-infinite cylinder and double the result, the transverse induced velocity from trailing wake vortex distribution is obtained.

$$v_{iy_{yx}}(x_A) = \frac{\Gamma_0 R \sin \phi}{2\pi^2} \int_{-\infty}^0 \frac{dx}{[R^2 + (x - x_A)^2]^{3/2}} \quad (14)$$

$$v_{iy_{yx}}(\bar{x}_A) = \frac{\Gamma_0 \sin \phi}{2\pi^2 R} \left(1 - \frac{\bar{x}_A}{\sqrt{1 + \bar{x}_A^2}} \right) \quad (15)$$

Finally the centreline transverse induced velocity can be obtained by combining equations 10 and 15.

$$v_{iy}(\bar{x}_A) = \frac{\Gamma_0}{2\pi^2 R} \left[\left(1 - \frac{\bar{x}_A}{\sqrt{1 + \bar{x}_A^2}} \right) \sin \phi - \frac{1}{\bar{x}_A \sqrt{1 + \bar{x}_A^2}} \right] \quad (16)$$

4.2 Deformed Centreline Equation

To obtain an analytical approximation of centreline equation, axial induced velocity v_{ia} obtained from vortex system is needed. It is calculated in a similar way, and a detailed derivation can also be found in McCormick.¹⁸ For brevity, the expression is given in equation 17.

$$v_{ia}(\bar{x}) = -\frac{\Gamma_0 \cos \phi}{4\pi R} \left(1 - \frac{\bar{x}}{\sqrt{1 + \bar{x}^2}} \right) \quad (17)$$

With equation 17 and 16, the deformed centreline can be expressed by considering it to be a surface streamline.

$$\frac{d\bar{y}}{v_y(\bar{x})} = \frac{d\bar{x}}{v_x(\bar{x})} \quad (18)$$

Local transverse velocity v_y and axial velocity v_x is given in equation 19.

$$\begin{aligned} v_y(\bar{x}) &= v_{iy}(\bar{x}) \\ v_x(\bar{x}) &= -V_\infty + v_{ia}(\bar{x}) \end{aligned} \quad (19)$$

The negative sign in front of V_∞ is because positive x is defined to be upstream, which is opposite to conventional freestream direction. Thus the deformed centreline equation 20 can be approximated by integrating equation 18.

$$\bar{y}(\bar{x}) = \begin{cases} 0 & \bar{x}_{LE} \leq \bar{x} \\ \int_{\bar{x}_{LE}}^{\bar{x}} \frac{v_{iy}(s)}{-V_\infty + v_{ix}(s)} ds & \bar{x}_{TE} \leq \bar{x} < \bar{x}_{TE} \\ \int_{\bar{x}_{LE}}^{\bar{x}_{TE}} \frac{v_{iy}(s)}{-V_\infty + v_{ix}(s)} ds + \frac{v_{iy}(\bar{x}_{TE})}{-V_\infty + v_{ix}(\bar{x}_{TE})} (\bar{x} - \bar{x}_{TE}) & \bar{x} < \bar{x}_{TE} \end{cases} \quad (20)$$

Equation 20 contains two parts : the first term represents the deformation on top of the wing starting from non-dimensional leading edge \bar{x}_{LE} until trailing edge \bar{x}_{TE} ; the second term assumes constant centreline deviation angle from rotation axis after trailing edge, and thus the transverse displacement is linear with downstream location \bar{x} .

The analytical expression of deformed centreline equation will be presented in two parts : the first part is for static case where $V_\infty = 0$ and the second part is for cases where $V_\infty > 0$

4.2.1 Deformed centreline equation in static condition

When $V_\infty = 0$ and $\bar{x} < \bar{x}_{TE}$, equation 20 simplifies to equation 21.

$$\begin{aligned} \bar{y}(\bar{x}) &= -\int_{\bar{x}_{LE}}^{\bar{x}_{TE}} \frac{v_{iy}(s)}{v_{ix}(s)} ds + \frac{v_{iy}(\bar{x}_{TE})}{v_{ix}(\bar{x}_{TE})} (\bar{x} - \bar{x}_{TE}) \\ &= -\frac{2}{\pi} \tan \phi (\bar{x} - \bar{x}_{LE}) + \frac{2}{\pi} \sec \phi \left[\frac{\bar{x} - \bar{x}_{TE}}{\bar{x}_{TE} (\sqrt{1 + \bar{x}_{TE}^2} - \bar{x}_{TE})} + \int_{\bar{x}_{LE}}^{\bar{x}_{TE}} \frac{ds}{s (\sqrt{1 + s^2} - s)} \right] \end{aligned} \quad (21)$$

Before proceed further, it is worth mentioning that the different factors affecting centreline deformation can be clearly observed in the last line of equation 21. The first term includes all contribution from streamwise vortices in the trailing wake, and it is a linear term in streamwise coordinate with proportional constant determined by helix angle. The second term represents the influence from blade circulation. This term grows with the proximity from leading edge to rotor plane. It is interesting to conclude that for a given geometry (\bar{x}_{LE} and \bar{x}_{TE}) in static condition, the deformed centreline shape only depends on wake helix angle ϕ .

Solving the integral and also consider all $\bar{x} < 0$, the complete static deformed centreline equation is given in equation 22.

$$\bar{y}(\bar{x}) = \begin{cases} 0, & \bar{x}_{LE} \leq \bar{x} \\ \frac{2}{\pi} (\sec \phi - \tan \phi) (\bar{x} - \bar{x}_{LE}) & \bar{x}_{TE} \leq \bar{x}, \\ + \frac{2}{\pi} \sec \phi \left(\sqrt{1 + \bar{x}^2} - \sqrt{1 + \bar{x}_{LE}^2} + \ln \left| \frac{\bar{x}_{LE}}{\bar{x}} \frac{1 - \sqrt{1 + \bar{x}^2}}{1 - \sqrt{1 + \bar{x}_{LE}^2}} \right| \right), & \bar{x} < \bar{x}_{LE} \\ \frac{2}{\pi} (\sec \phi - \tan \phi) (\bar{x}_{TE} - \bar{x}_{LE}) & \\ + \frac{2}{\pi} \sec \phi \left(\sqrt{1 + \bar{x}_{TE}^2} - \sqrt{1 + \bar{x}_{LE}^2} + \ln \left| \frac{\bar{x}_{LE}}{\bar{x}_{TE}} \frac{1 - \sqrt{1 + \bar{x}_{TE}^2}}{1 - \sqrt{1 + \bar{x}_{LE}^2}} \right| \right) & \bar{x} < \bar{x}_{TE} \\ - \frac{2}{\pi} \left[\tan \phi (\bar{x} - \bar{x}_{LE}) - \frac{\bar{x} - \bar{x}_{TE}}{\bar{x}_{TE} (\sqrt{1 + \bar{x}_{TE}^2} - \bar{x}_{TE})} \sec \phi \right], & \end{cases} \quad (22)$$

4.2.2 Deformed centreline equation in forward flight

When $V_\infty > 0$, the slipstream will be convected in streamwise direction, which tends to attenuate centreline deformation. From equation 20, the integral term is expanded.

$$I(\bar{x}) = \int_{\bar{x}_{LE}}^{\bar{x}} \frac{v_{iy}(s)}{-V_\infty + v_{ix}(s)} ds = -\frac{2}{\pi} \int_{\bar{x}_{LE}}^{\bar{x}} \frac{\tan \phi - \frac{\sec \phi}{s(\sqrt{1+s^2}-s)}}{1 + \frac{\sqrt{1+s^2} \sec \phi}{\bar{\Gamma}_0(\sqrt{1+s^2}-s)}} ds \quad (23)$$

where the non-dimensional circulation $\bar{\Gamma}_0 = \frac{\Gamma_0}{4\pi V_\infty R}$. Since Γ_0 is associated with the total propeller thrust, the centreline deformation in forward flight condition is determined by both disk loading and total thrust condition. The relations between propeller thrusting condition and slipstream parameters $\phi, \bar{\Gamma}_0$ are related from vortex theory.¹⁸

$$\tan \phi = -\frac{V_\infty + v_{ia}}{\Omega R} = \frac{1}{2\pi} \left(\sqrt{\frac{8C_T}{\pi} + J^2} - J \right) \quad (24)$$

Complete the integrations of $\tan \phi$ and $\sec \phi$ terms.

$$\begin{aligned} I(\bar{x}) = & -\frac{2\bar{\Gamma}_0 \sin \phi}{\pi} \frac{1}{2a-1} \left[(\bar{x} - \bar{x}_{LE}) - \left(\sqrt{1 + \bar{x}^2} - \sqrt{1 + \bar{x}_{LE}^2} \right) \right] \\ & - \frac{2(\bar{\Gamma}_0 \cos \phi)^2}{\pi \sqrt{2a-1}} \left(\frac{\tan \phi}{2a-1} - \frac{\sec \phi}{a} \right) \left[\tan^{-1} \left(\bar{x} \frac{\sqrt{2a-1}}{a} \right) - \tan^{-1} \left(\bar{x}_{LE} \frac{\sqrt{2a-1}}{a} \right) \right] \\ & + \tan^{-1} \frac{\sqrt{(2a-1)(1 + \bar{x}^2)}}{a-1} - \tan^{-1} \frac{\sqrt{(2a-1)(1 + \bar{x}_{LE}^2)}}{a-1} \\ & + \frac{\bar{\Gamma}_0}{\pi a} \ln \left| \frac{\sqrt{1 + \bar{x}^2} - 1}{\sqrt{1 + \bar{x}^2} + 1} \frac{\sqrt{1 + \bar{x}_{LE}^2} + 1}{\sqrt{1 + \bar{x}_{LE}^2} - 1} \right| \end{aligned} \quad (25)$$

where $a = 1 + \bar{\Gamma}_0 \cos \phi$.

The complete deformed centreline equation in forward flight condition is in equation 26.

$$\bar{y}(\bar{x}) = \begin{cases} 0, & \bar{x}_{LE} \leq \bar{x} \\ -\frac{2}{\pi}\bar{\Gamma}_0 \cos \phi \left\{ \frac{\tan \phi}{2a-1} \left[\bar{x} - \bar{x}_{LE} - \left(\sqrt{1+\bar{x}^2} - \sqrt{1+\bar{x}_{LE}^2} \right) \right] \right. \\ \quad + \frac{\bar{\Gamma}_0 \cos \phi}{\sqrt{2a-1}} \left(\frac{\tan \phi}{2a-1} - \frac{\sec \phi}{a} \right) [\psi(\bar{x}) + \xi(\bar{x}) - \psi(\bar{x}_{LE}) - \xi(\bar{x}_{LE})] & \bar{x}_{TE} \leq \bar{x} < \bar{x}_{LE} \\ \quad \left. - \frac{\sec \phi}{2a} \ln \left| \frac{\sqrt{1+\bar{x}^2}-1}{\sqrt{1+\bar{x}^2}+1} \frac{\sqrt{1+\bar{x}_{LE}^2}+1}{\sqrt{1+\bar{x}_{LE}^2}-1} \right| \right\}, \\ \\ -\frac{2}{\pi}\bar{\Gamma}_0 \cos \phi \left\{ \frac{\tan \phi}{2a-1} \left[\bar{x}_{TE} - \bar{x}_{LE} - \left(\sqrt{1+\bar{x}_{TE}^2} - \sqrt{1+\bar{x}_{LE}^2} \right) \right] \right. \\ \quad + \frac{\bar{\Gamma}_0 \cos \phi}{\sqrt{2a-1}} \left(\frac{\tan \phi}{2a-1} - \frac{\sec \phi}{a} \right) [\psi(\bar{x}_{TE}) + \xi(\bar{x}_{TE}) - \psi(\bar{x}_{LE}) - \xi(\bar{x}_{LE})] \\ \quad \left. - \frac{\sec \phi}{2a} \ln \left| \frac{\sqrt{1+\bar{x}_{TE}^2}-1}{\sqrt{1+\bar{x}_{TE}^2}+1} \frac{\sqrt{1+\bar{x}_{LE}^2}+1}{\sqrt{1+\bar{x}_{LE}^2}-1} \right| \right\} & \bar{x} < \bar{x}_{TE} \\ -\frac{2\bar{\Gamma}_0}{\pi} \frac{\sin \phi \left(\sqrt{1+\bar{x}_{TE}^2} - \bar{x}_{TE} \right) - 1/\bar{x}_{TE}}{a\sqrt{1+\bar{x}_{TE}^2} - (a-1)\bar{x}_{TE}} (\bar{x} - \bar{x}_{TE}) \end{cases} \quad (26)$$

where $\psi(\bar{x}) = \tan^{-1} \frac{\bar{x}\sqrt{2a-1}}{a}$, $\xi(\bar{x}) = \tan^{-1} \frac{\sqrt{(2a-1)(1+\bar{x}^2)}}{a-1}$.

4.3 Validation with Wake Survey

Transverse displacement of slipstream wasn't directly measured by the five-hole probe. Cross-flow strain rate was calculated from velocity distribution instead to determine a more precise geometry of the deformed slipstream. Assuming x derivatives of cross-flow flow components were small relative to y and z derivatives of streamwise flow, the cross-flow strain rate can be calculated from equation 4.3.

$$\epsilon_{\perp} = \sqrt{\left(\frac{\partial u}{\partial y}\right)^2 + \left(\frac{\partial u}{\partial z}\right)^2} \quad (27)$$

Locus of maximum shear stress was determined to be the outer edge of slipstream, as demonstrated in Figure 12.

Suppose the highest point of upper slipstream boundary is (y_1, z_1) and the lowest point of lower slipstream boundary is (y_2, z_2) , the transverse displacement is calculated as half of the spanwise distance between the two points.

$$y_{disp} = \frac{|y_2 - y_1|}{2} \quad (28)$$

Calculated slipstream transverse displacements under three advance ratios were compared with the derived theoretical trajectory in Figure 13.

The trajectories were given as functions of downstream location. Markers representing centreline displacements from experimental data were placed at $\bar{z} = 3.4$, where the survey plane was located. The plots were colour-coded for different advance ratios. A static case with $J = 0$ was also plotted for reference.

Theoretical trajectories varied significantly with changes in advance ratio. The displacement reduces from a theoretical value of $43\%R$ at static condition to $8\%R$ at $J = 0.6$. This is caused by two phenomena : 1) a larger freestream convects propeller wake faster downstream and the slipstream will displace less in the same distance ; 2) propeller thrust loading reduces with advance ratio and thus the streamwise vortices system is weaker. The first phenomenon is largely dominant.

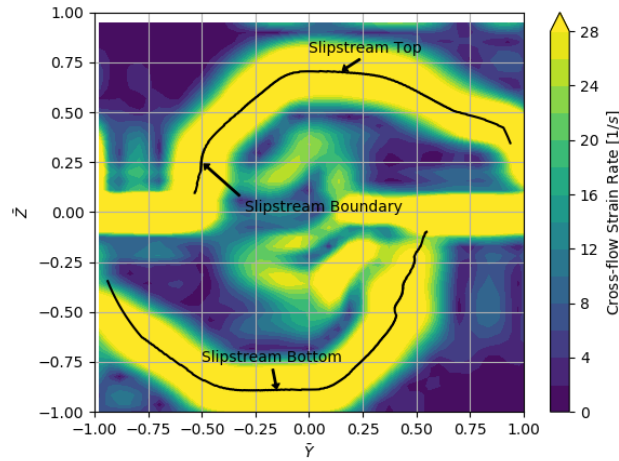


Figure 12: Transverse shear stress distribution in survey plane at $J = 0.6$

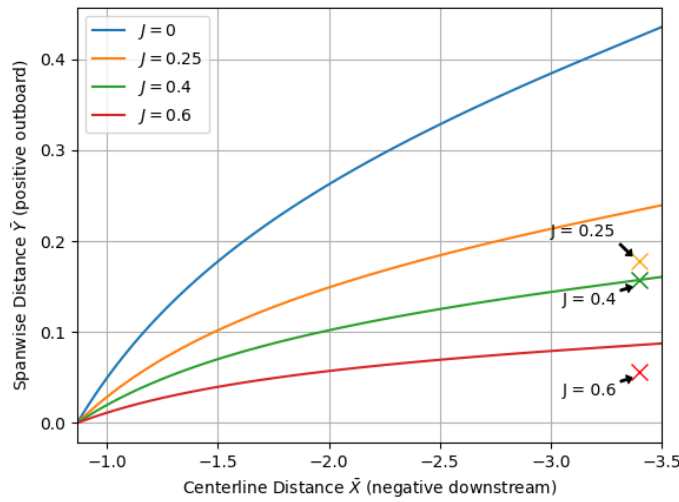


Figure 13: Displaced slipstream centreline

When compared with data extracted from experimental data, agreement is observed for $J = 0.4$ and $J = 0.6$. However the slipstream displacement at $J = 0.25$ appeared to be overestimated by analytical model. A closer examination of Figure 3 indicates that while left extremity of upper slipstream boundary deviated more at $J = 0.25$ than at $J = 0.4$, the spanwise distance between slipstream top and bottom didn't vary as much. This is most likely due to viscous mixture near the slipstream top and bottom boundaries, which makes determination of the exact slipstream displacement difficult. Furthermore, as mentioned in section 3, onset of local stall on blown wing section may also obstruct direct comparison with theoretical wake displacement.

5. Conclusions

Experimental results from a wake survey behind propeller-wing combination at ENAC low-speed windtunnel has been presented. The result suggested significant slipstream deformation characterised by transverse placement at reducing advance ratio. The phenomenon was induced due to the non-penetration condition at wing surface and the velocity differences in the displaced region may alter lifting performance of the affected sections.

Comparisons with two propeller slipstream models revealed differences in flow structure. Neither models was able to satisfactorily produce flowfield downstream the propeller-wing combination. Model from Goates et al however considered additional wing induced velocity, and provided a more detailed velocity distribution within slipstream. Modelling of transverse slipstream displacement was lacking in both models.

An analytical model was proposed at the end to include the wing effect on propeller slipstream development

in reduced-order model for propeller-wing analysis. The model depends on advance ratio and thrust coefficient on propeller. Its fully analytical form allows rapid calculation.

6. Acknowledgments

The work was conducted as a joint project between research institutes ISAE-Supaéro, ENAC and Delair company, with partial funding from Association Nationale de la Recherche et de la Technologie. The authors would like to express gratitude to Mr. Stéphane Terrenoir for his coordination of the project, to engineers at Delair, Mr. Alexandre Lapadu, Mr. Clément Pfiffer and colleagues at ENAC, Mr. Michel Gorraz, Mr. Xavier Paris, Mr. Nicolas Peteilh for their professional assistance and expertise during the implementation and execution of wind tunnel experiment.

References

- [1] Paul J Weitz. A qualitative discussion of the stability and control of vtol aircraft during hover (out of ground effect) and transition. Technical report, NAVAL POSTGRADUATE SCHOOL MONTEREY CA, 1964.
- [2] Paul F Yaggy and Vernon L Rogallo. A wind-tunnel investigation of three propellers through an angle-of-attack range from 0 deg to 85 deg. Technical Report NACA-TN-D-318, NASA Ames Research Center, Moffett Field, CA, United States, May 1960.
- [3] John De Young. Propeller at high incidence. *Journal of Aircraft*, 2(3):241–250, 1965.
- [4] Yuchen Leng, Heesik Yoo, Thierry Jardin, Murat Bronz, and Jean-Marc Moschetta. Aerodynamic modeling of propeller forces and moments at high angle of incidence. In *AIAA Scitech 2019 Forum*, page 1332, 2019.
- [5] Leandro Ribero Lustosa, François Defaj, and Jean-Marc Moschetta. Development of the flight model of a tilt-body mav. Toulouse, France, August 2014. International Micro Air Vehicle Conference and Competition.
- [6] Murat Bronz, Ewoud J Smeur, Hector Garcia de Marina, and Gautier Hattenberger. Development of a fixed-wing mini uav with transitioning flight capability. Atlanta, United States, June 2017. 35th AIAA Applied Aerodynamics Conference, AIAA AVIATION Forum.
- [7] R Hugh Stone. Aerodynamic modeling of the wing-propeller interaction for a tail-sitter unmanned air vehicle. *Journal of Aircraft*, 45(1):198–210, 2008.
- [8] WF Phillips. Propeller momentum theory with slipstream rotation. *Journal of aircraft*, 39(1):184–187, 2002.
- [9] Waqas Khan and Meyer Nahon. Improvement and validation of a propeller slipstream model for small unmanned aerial vehicles. In *Unmanned Aircraft Systems (ICUAS), 2014 International Conference on*, pages 808–814. IEEE, 2014.
- [10] Joshua Taylor Goates. Development of an improved low-order model for propeller-wing interactions. 2018.
- [11] Kitso Epema. Wing optimisation for tractor propeller configurations: Validation and application of low-order numerical models adapted to include propeller-induced velocities. 2017.
- [12] LLM Veldhuis. Review of propeller-wing aerodynamic interference. In *24th International Congress of the Aeronautical Sciences*, volume 6, 2004.
- [13] Bruce A Reichert and Bruce J Wendt. A new algorithm for five-hole probe calibration, data reduction, and uncertainty analysis. 1994.
- [14] Jens Nørkær Sørensen. *General momentum theory for horizontal axis wind turbines*, volume 4. Springer, 2016.
- [15] Dave P Witkowski, Alex KH Lee, and John P Sullivan. Aerodynamic interaction between propellers and wings. *Journal of Aircraft*, 26(9):829–836, 1989.
- [16] Apc propeller performance data. <https://www.apcprop.com/technical-information/performance-data/>, [Online; accessed 21-May-2019].
- [17] Warren F Phillips. *Mechanics of flight*. John Wiley & Sons, 2004.
- [18] B.W. McCormick. *Aerodynamics, Aeronautics, and Flight Mechanics*. Wiley, 1994.